Hindawi
Advances in Civil Engineering
Volume 2023, Article ID 1408320, 16 pages
https://doi.org/10.1155/2023/1408320

Research Article

Experimental, Numerical, and Analytical Studies of Uniaxial Compressive Behavior of Concrete Confined by Ultra-High-Performance Concrete

Shijun Wang,[1] Chun Liu,[1] Yunfei Tian,[1] Xing Wang,[1] Teng Tong ,[2] and Saiyang Zhuo [2]

[1]*Division of Development, Gansu Electric Power Corporation, State Grid, Lanzhou, China*
[2]*School of Civil Engineering, Southeast University, Nanjing, China*

Correspondence should be addressed to Saiyang Zhuo; saiyangzhuo@gmail.com

Received 6 December 2022; Revised 28 February 2023; Accepted 25 March 2023; Published 8 May 2023

Academic Editor: Payam Shafigh

This research examines the uniaxial behavior of core concrete, which is confined by a UHPC (ultra-high-performance concrete) shell, through experimental, numerical, and analytical methods. Various configurations, including different UHPC shell shapes, thicknesses, and core concrete compressive strengths, were tested until failure occurred. Results indicate that the UHPC shell altered the failure modes and enhanced the maximum stress and corresponding strain in uniaxial loading. Additionally, in square and rectangular specimens, debonding between the UHPC and NC (normal concrete) interfaces was observed. Furthermore, we constructed numerical models which integrate the concrete damage plasticity model for NC/UHPC and the coupled adhesive-frictional model implemented in cohesive elements. The model accurately reflects the crack and debonding evolution of the tested specimen. Subsequently, an analytical stress-strain model for uniaxial loading was created based on the experimental results. The confining pressure for square/rectangular specimens was determined using Airy's function. The validity of the analytical model was verified by comparing its predictions with the experimental results.

1. Introduction

Concrete bridge piers play a significant role in supporting the bridge superstructure and resisting ship/vehicle collision and earthquakes [1, 2]. In the medium- and high-seismicity zones, the design and detailing of concrete piers are essential to maintain a bridge's overall performance during an earthquake. Lessons from past earthquake events indicate that strengthening the concrete bridge piers is necessary, especially for those completed a few decades ago as per the former version of the design code.

The current design philosophies are to guarantee the deformation capacity of preselected regions, i.e., the plastic hinge zone. To this end, the plastic hinge zone of a concrete pier necessitates adequately confined core concrete and sufficiently anchored flexural rebars [3]. Stirrups with minimal spacing can provide an excellent confining effect for the core concrete, thus enhancing its strength and ductility. In addition, for these existing bridges, another solution to strengthen the core concrete is to jacket the concrete piers. For instance, bridge piers with a steel jacket [4] or a fiber-reinforced polymer (FRP) jacket [5] both show improved seismic behaviors. However, extensive application of these jacketing solutions is limited due to their poor long-term durability and FRP-concrete separation [6].

Ultra-high-performance concrete (UHPC) is a novel cementitious material notable for its outstanding mechanical and durability characteristics [7]. These enhanced properties render UHPC competitive in the bridge community, i.e., accelerated bridge construction [8], bridge deck retrofit [9], bridge widening [10], and seismic pier retrofit [1, 2]. Multiple pseudocyclic loading tests performed on concrete piers [11] have demonstrated that the UHPC jacket effectively suppresses the crushing of core concrete and increases the deformation capacity of bridge piers. Similar findings are also reported by other researchers [12–15].

Although the aforementioned studies investigated the seismic behavior of normal concrete piers strengthened with UHPC shells, only a few studies contributed to the quantification of the confinement effect provided by the UHPC jacket on the core concrete, which requires further investigation. Xie et al. [16] pioneered testing eighteen circular and square concrete columns confined by the UHPC shell. The 300 mm-height specimens were reinforced with UHPC shell thicknesses ranging between 20 mm and 40 mm. The cracking of the UHPC shell was witnessed in their test without UHPC-NC debonding. Their core concrete owned compressive strength of 41.3 MPa, and apparent increases in strength and ductility were obtained. Ali Dadvar et al. [17] subsequently investigated 14 circular columns with UHPC jackets that had various surface treatments, such as grooving, abrasion, and sandblasting. The results of the study showed that longitudinal grooving significantly improved the columns' load-bearing capacity and energy absorption capabilities. Recently, Ronanki and Aaleti [3] loaded the circular (228 mm~280 mm in diameter) and square (203~305 mm in length) specimens to failure, using core concrete with compressive strengths varying between 18.15 and 26.57 MPa. The study findings demonstrated that the unreinforced UHPC shell confinement led to a significant increase in both peak compressive stress (15%~30%) and crushing strain (26%~46%) of the core concrete. Moreover, these specimens exhibited a failure pattern characterized by cracking of the UHPC shell without debonding of the interface.

Despite the aforementioned contributions, there is minimal experimental and numerical research regarding the confinement of core concrete with UHPC shells. This limited number of specimens makes it difficult to comprehensively evaluate the behavior of UHPC-confined concrete, and there is currently no experimental data available for columns with rectangular cross sections. These research gaps have hindered the practical application of UHPC jackets in the retrofitting of RC components. Therefore, the objectives of this study are twofold: (1) to broaden the experimental knowledge of the uniaxial behavior of columns with UHPC confinement; and (2) to develop an analytical solution to predict the uniaxial stress-strain relationship of core concrete confined by the UHPC shell. To this end, another twelve specimens were prepared with various core concrete strengths, shapes, and UHPC thicknesses. In addition to the previous findings, our test indicated the critical role of the interface between UHPC and NC. Based on the experimental observations, we construct the numerical model accounting for the coupled adhesive-frictional interface model. Additionally, we have proposed an analytical solution for predicting the uniaxial stress-strain behavior of core concrete under the confinement of a UHPC shell.

2. Testing Details

2.1. Specimen Details. The following factors were considered to study the enhancement of the UHPC jacket/shell on the NC short columns, namely, the shape of the specimen (circular, square, and rectangular), the strength of core concrete (Grade C50 and C30), and the thickness of the UHPC shell (15 to 25 mm). To this end, twelve specimens were fabricated, covering the factors mentioned above, as shown in Table 1.

Their geometric details are further illustrated in Figure 1. The heights of the core concrete columns for circular and square/rectangular specimens were 600 mm and 450 mm, respectively. The circular core columns had a diameter of 250 mm for their cross section, while the square and rectangular core columns were $200\,\text{mm} \times 200\,\text{mm}$ and $200\,\text{mm} \times 150\,\text{mm}$, respectively. To assess the efficacy of UHPC confinement in improving the axial compressive behavior of the core NC columns, the UHPC shell was designed to be 20 mm shorter (Figure 1) than the core NC portion, ensuring that the compressive load was not directly transmitted to the UHPC shell.

The specimen fabrication is illustrated in Figure 2. Firstly, the core concrete short columns were prepared, as shown in Figure 2(a). Subsequently, the UHPC shell was poured around the core part (Figure 2) and heat-treated for three days to gain rapid strength development in UHPC. It is noted that before casting the UHPC material, the core NC part was merged into the water for 12 hours to gain a better UHPC-NC bond strength. The specimens were demolded (Figure 2) and cured at 40°C and 99% relative humidity for another two days. Before the test loading, the top and bottom surfaces of the specimens were leveled and oiled.

2.2. Materials. As shown in Table 1, the C30 and C50 concrete were chosen for the core NC columns, as per Chinese code [18]. Eighteen concrete cubes of 150 mm length were loaded to failure. The mean cubic (f'_{cu}) and equivalent cylindrical (f'_c) strengths were $f'_{cu}/f'_c = 33.7/26.7$ MPa for C30 concrete and $f'_{cu}/f'_c = 48.7/38.5$ MPa for C50 concrete, respectively. The standard deviations of C30 and C50 concrete were 2.1 MPa and 3.2 MPa, respectively.

Commercial UHPC was adopted for the shell, and one cubic meter UHPC consisted of 2095 kg premixed powder, 156 kg steel fibers, 182.4 kg water, and 22.10 kg polycarboxylate superplasticizer. In the chosen UHPC, the coarse aggregates were eliminated, and only fine aggregates were selected. The maximum aggregate size did not exceed 1.20 mm. To mitigate the quite brittle behavior after the occurrence of minor cracks, the straight brass coating steel fibers were employed, with 0.2 mm in diameter and 20 mm in length, and they took about a 2% volume fraction of the hardened UHPC paste. The mixture proportions for NC (C30 and C50) and UHPC are presented in Tables 2 and 3.

The tensile properties of UHPC were evaluated using dog bone-shaped specimens, as depicted in Figure 3. The average tensile capacity of UHPC was measured to be 5.6 MPa. It was observed that the UHPC material maintained its tensile strength beyond a strain value of 0.002. The mean cubic (f'_{cu}) strength of UHPC was around 156.9 MPa, obtained from six 100 mm-length cubes, with the standard deviation of 4.8 MPa. Moreover, three $1000\,\text{mm} \times 1000\,\text{mm} \times 300\,\text{mm}$ prisms were tested, of which the mean cylindric strength was

Table 1: Geometry and property details for these specimens.

Specimens	Shape	Quantity	Core concrete (MPa)	UHPC thickness (mm)	Peak strength (MPa)		Corresponding strain	
					f'^{*}_{cc}	Rise (%)	ε^{*}_{cc}	Rise (%)
CU-C50	Circular	3	38.5	0	—	—	—	—
CC-C50-U25		2		25	57.1	56	0.0036	89
					54.0	47	0.0035	83
SU-C50	Square	3	38.5	0	—	—	—	—
SC-C50-U25		2		25	51.3	31	0.0038	81
					58.8	50	0.0039	88
RU-C50	Square	3	38.5	0	—	—	—	—
RC-C50-U15		1		15	43.3	10	0.0034	72
RC-C50-U20		1		20	46.7	19	0.0036	80
RC-C50-U25		1		25	50.0	27	0.0037	82
RC-C30-U15		1	26.7	15	31.7	18	0.0036	78
RC-C30-U20		1		20	33.3	24	0.0037	83

Note. The legend for the specimen is defined as follows: CC = circular confined; CU = circular unconfined; SC = square confined; SU = square unconfined; RC = rectangular confined; RU = rectangular unconfined.

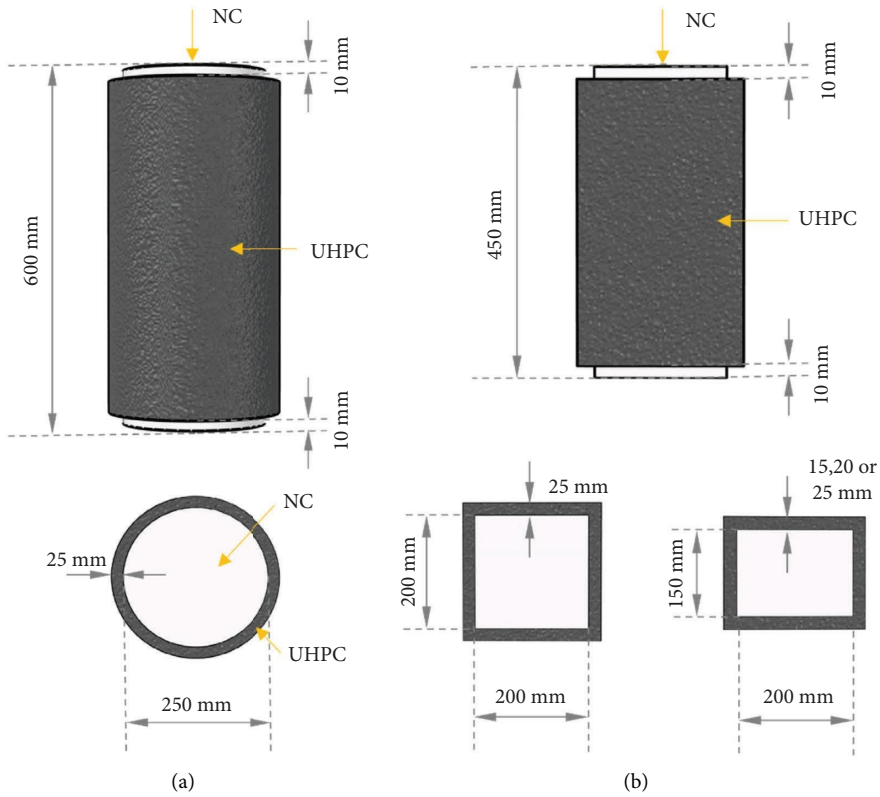

Figure 1: Geometries of the core concrete columns confined by UHPC shells (unit: mm). (a) Circular specimens. (b) Square and rectangular specimens.

around 116.1 MPa, and the elastic modulus was measured as 55.6 GPa.

To characterize the behavior of the UHPC-NC interface, nine additional specimens were prepared for slant shear testing, in addition to the UHPC and NC materials. For the sake of brevity, the experimental details are not presented here and can be found in Yuan et al. [19]. The average adhesion force was $c = 1.2$ MPa, and the frictional coefficient was $\mu = 1.0$.

2.3. Test Setup. The test setup is depicted in Figure 4. Conventional foil strain gauges were attached longitudinally and transversely to the specimens. The specimens were then loaded uniaxially using a 5000 kN capacity MTS machine.

(a) (b) (c)

Figure 2: Fabrication of tested specimens. (a) Core concrete columns. (b) Pouring the UHPC shell. (c) Demolding.

Table 2: Proportions of NC mixture per cubic meter.

	Water (kg)	Cement (kg)	Sand (kg)	Gravel (kg)	Water (kg)
C30	175	461	512	1252	175
C50	205	488	562	1195	205

Table 3: Proportions of UHPC mixture per cubic meter.

	UHPC powder (kg)	Steel fiber (kg)	Superplasticizer (kg)	Water (kg)	Volume fraction of steel fiber (%)
Mixture	2095	156	22.1	182.4	2

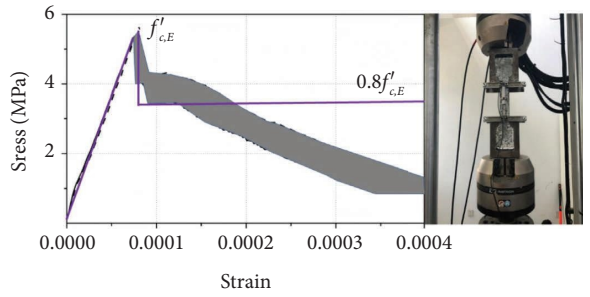

Figure 3: Experimental and assumed tensile behavior of the UHPC material.

The specimens were fixed at the bottom support, and oil was applied to the top and bottom surfaces to ensure smooth loading. All specimens were subjected to force-controlled loading. The loading rate was maintained slowly (5 kN/min) to eliminate the rate effect. The load increment was 50 kN and maintained at least 10 minutes. Due to the force-controlled scheme, postpeak behaviors of the specimens were not obtained in our test.

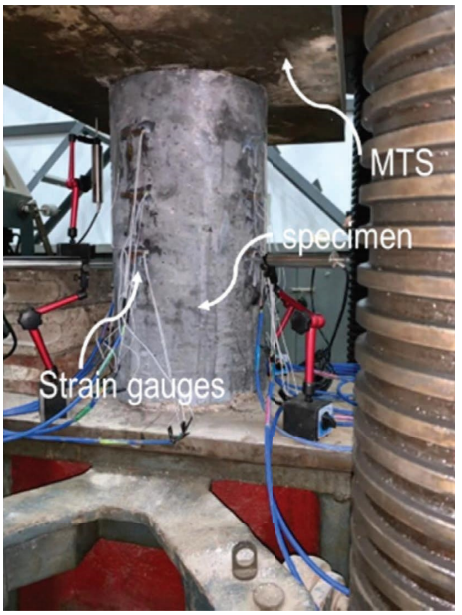

Figure 4: Test setup.

3. Finite Element Modeling

3.1. Description of the Numerical Model. A detailed 3D model was developed for numerical simulation to investigate the uniaxial compressive behavior of confined core concrete columns. The implicit finite element method was employed using commercial software Abaqus/Standard [20], with all components modeled using nonlinear material properties.

The mechanical behavior of the core concrete and the UHPC shell was simulated using the concrete damage plasticity (CDP) model in Abaqus software. The stress-strain relationship was defined based on the compressive strength obtained from experimental data. As debonding was observed at the UHPC-NC interface (Section 5.1), a zero-thickness cohesive element was deliberately inserted between the core concrete column and the UHPC shell, as illustrated in Figure 5.

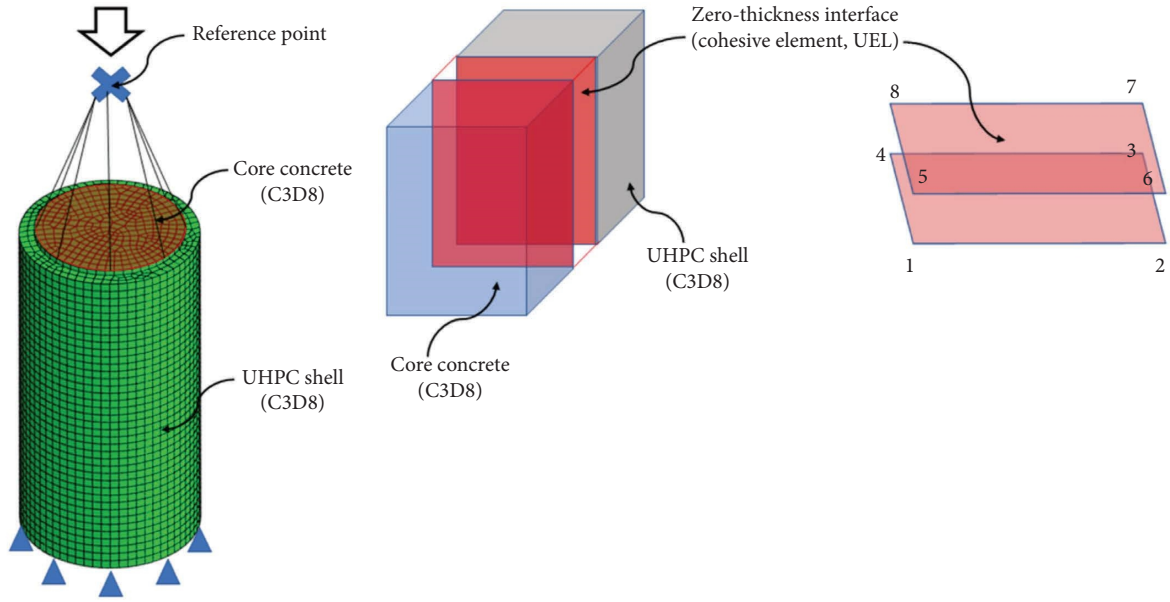

Figure 5: Illustration of the finite element model. (a) The boundary condition. (b) The zero-thickness cohesive element.

In the FE model, the core concrete and UHPC shell specimens were modeled using 8-noded brick elements, with a characteristic mesh size varying from 20 mm to 25 mm, as illustrated in Figure 5. The model was subjected to a prescribed deformation on its top surface while being vertically constrained at the bottom to simulate loading conditions. The centroid node of the bottom surface is also constrained in the plane direction to avoid rigid motion. The zero-thickness cohesive element is also illustrated in Figure 5 for the simulation of UHPC-NC interfacial behavior.

3.2. CDP Model for UHPC and Concrete. Monteiro and Lubliner [21] first proposed the CDP model, and later it was modified by Lee and Fenves [22] to reflect the cyclic behavior of cementitious materials further. In the CDP model, the second-order strain tensor ε could be decomposed into the elastic part ε_e and the plastic part ε_p, as follows:

$$\boldsymbol{\varepsilon} = \boldsymbol{\varepsilon}_e - \boldsymbol{\varepsilon}_p. \tag{1}$$

The second-order effective stress tensor $\overline{\sigma}$, on the skeleton of the material, follows the generalized Hook's law, as follows:

$$\begin{aligned} \overline{\boldsymbol{\sigma}} &= \mathbb{C}: \boldsymbol{\varepsilon}_e \\ &= \mathbb{C}: \left(\boldsymbol{\varepsilon} - \boldsymbol{\varepsilon}_p\right), \end{aligned} \tag{2}$$

where $\mathbb{C}$ is the fourth-order undamaged elastic stiffness tensor.

Therewith, the second-order stress tensor σ on the damage body is linked to the effective one $\overline{\sigma}$ through the scalar damage variable d, as follows:

$$\begin{aligned} \boldsymbol{\sigma} &= (1-d)\overline{\boldsymbol{\sigma}} \\ &= (1-d)\mathbb{C}: \boldsymbol{\varepsilon}_e. \end{aligned} \tag{3}$$

The damage variable d is a function of the stress state and depends on another two damage variables, as follows:

$$d = 1 - \left(1 - s^{+}d^{+}\right)\left(1 - s^{-}d^{-}\right), \tag{4}$$

where d^{+} and d^{-} are damage variables for tension and compression, respectively; s^{+} and s^{-} accounts for the tensile and compressive stiffness recovery effects, respectively. The detailed expression for these variables (s^{+}, s^{-}, d^{+}, d^{-}, ε_p, and $\mathbb{C}$) are not presented for brevity, and the reader could refer to the Abaqus theoretical manual [20].

The CDP model requires the uniaxial tensile and compressive stress-strain behaviors as the input parameter. For compressive behavior, the following model proposed by Hognestad et al. [23] is adopted for concrete and UHPC materials:

$$\begin{aligned} \sigma &= f_c\left[2\frac{\varepsilon_c}{\varepsilon_{co}} - \left(\frac{\varepsilon_c}{\varepsilon_{co}}\right)^2\right] \text{for } 0 < \varepsilon_c < 0.002, \\ \sigma &= 2f_c\frac{\left(\varepsilon_c/\varepsilon_{co}\right)}{1 + \left(\varepsilon_c/\varepsilon_{co}\right)^2} \text{ for } 0.002 < \varepsilon_c < 0.0035, \end{aligned} \tag{5}$$

where σ and ε_c represent the compressive stress and strain of normal concrete or UHPC, respectively. Meanwhile, f_c denotes the ultimate compressive strength of concrete; ε_{co} denotes the strain corresponding to f_c.

The finite element model is assigned with the tensile behavior of concrete and UHPC using the fracture energy cracking model, where the fracture energy for concrete is obtained from CEB-FIP [24] as follows:

$$G_f = G_{f0}\left(\frac{f_c}{10}\right)^{0.7}, \tag{6}$$

where G_{f0} is the fracture energy (=0.03 N/mm) since the diameter of the coarse aggregate of core concrete is about 16 mm. It is noted that equation (6) is not applicable to UHPC, and $G_f = 0.95\,\text{N/mm}^2$ is adopted for the UHPC material [25].

In order to facilitate the potential users, the relevant parameters for the core concrete and the UHPC shell are given in Table 4.

3.3. Cohesive Element for the UHPC-NC Interface. The 8-noded cohesive element is deliberatively inserted between the adjacent 3D solid elements (C3D8) at the interface. In the unstressed state, the cohesive element's two surfaces are in close contact and have zero thickness.

To complete the definition of the cohesive element, we define the nodal displacement vector $\widetilde{u}_{\text{gol}}$ (24×1) as follows:

$$\widetilde{u}_{\text{gol}} = \left[u_x^1, u_y^1, u_z^1, u_x^2, u_y^2, u_z^2, \cdots, u_x^8, u_y^8, u_z^8\right]^T. \tag{7}$$

The rotational matrix $\mathbf{R}$ is a function of the normal vector $\overline{\mathbf{n}}$ and two perpendicular tangential vectors $\overline{\mathbf{t}}_2$ and $\overline{\mathbf{t}}_3$, obtained at the midplane of the cohesive element, as follows:

$$\mathbf{R} = \left\{\begin{array}{c} \overline{\mathbf{n}}^T \\ \overline{\mathbf{t}}_2^T \\ \overline{\mathbf{t}}_3^T \end{array}\right\}. \tag{8}$$

With the rotational matrix $\mathbf{R}$ at the hand, the global displacement vector $\widetilde{u}_{\text{gol}}$ could be easily transformed to the local one $\widetilde{u}_{\text{loc}}$.

Using the Galerkin method [26], the tangent stiffness matrix and the right-hand-side residual vector for the cohesive element is obtained as follows:

$$\begin{aligned} \mathbf{K}_{\text{el}} &= \int_0^1\int_0^1 \mathbf{B}^T\mathbf{R}^T\mathbf{D}_{\text{loc}}\mathbf{R}\mathbf{B}\det\mathbf{J}\,\mathrm{d}\xi\,\mathrm{d}\eta, \\ \mathbf{F}_{\text{el}} &= \int_0^1\int_0^1 \mathbf{B}^T\mathbf{R}^T\mathbf{t}_{\text{loc}}\det\mathbf{J}\,\mathrm{d}\xi\,\mathrm{d}\eta, \end{aligned} \tag{9}$$

where (ξ, η) denote the intrinsic coordinates, $\mathbf{J}$ denotes the Jacobian, $\mathbf{D}_{\text{loc}}$ is the local force vector, $\mathbf{t}_{\text{loc}}$ is the local force vector, and $\mathbf{B}$ is the global displacement-separation matrix.

The matrix $\mathbf{B}$ is calculated using the shape functions N_i $(i = 1, 2, \ldots, 8)$, as follows:

$$\mathbf{B} = \left[N_1\mathbf{I}_{3\times3}\middle|N_2\mathbf{I}_{3\times3}\middle|\cdots\middle|N_8\mathbf{I}_{3\times3}\right], \tag{10}$$

where $\mathbf{I}_{3\times3}$ is the identity matrix.

Furthermore, the local force vector $\mathbf{t}_{\text{loc}}$ is as follows:

Table 4: Relevant CDP parameters for core concrete and the UHPC shell.

	Concrete (C30)	Concrete (C50)	UHPC
E_c (GPa)	30.75	32.15	55.6
ν	0.20	0.20	0.20
χ	1.16	1.16	1.16
s^+	0	0	0
k^+	0.90	0.90	0.90
$f_c^+ = f_t$ (MPa)	2.16	3.16	5.6
s^-	1	1	1
k^-	0.50	0.50	0.50
$f_c^- = f_c'$ (MPa)	26.7	38.5	139.5
ψ	20	20	20

Note. The relevant definitions can refer to [20].

$$t_{\text{loc}}\Delta_t = \left\{\begin{array}{c} T_n \\ \dfrac{T_t\Delta_2}{\Delta_t} \\ \dfrac{T_t\Delta_3}{\Delta_t} \end{array}\right\}, \tag{11}$$

where the tangential opening directions are coupled through the relation $\Delta_t = \sqrt{\Delta_1^2 + \Delta_2^2}$; and T_n and T_t are normal and tangential tractions obtained from the following model.

3.4. Coupled Adhesive-Frictional Model. The slant shear test suggests that the tangential traction T_t of the UHPC-NC interface consists of two parts: (1) the adhesive force denoted by $T_{t,a}$ and (2) frictional force $T_{t,f}$, which are expressed as follows:

$$\begin{aligned} T_t &= T_{t,a} \text{ for } \Delta_n > 0, \\ T_t &= T_{t,a} + T_{t,f} \text{ for } \Delta_n \le 0. \end{aligned} \tag{12}$$

For the adhesive part, the normal traction T_n and tangential traction $T_{t,a}$ adopt the nonpotential formulas for the adhesion [27], as follows:

$$\begin{aligned} T_n(\Delta_n, \Delta_t) &= T_{n,\max}\exp(1)\frac{\Delta_n}{\delta_n}\exp\left(-\frac{\Delta_n}{\delta_n}\right)\exp\left(-\frac{\Delta_t^2}{\delta_t^2}\right) \text{ for } \Delta_n > 0, \\ T_n(\Delta_n, \Delta_t) &= 100T_{n,\max}\exp(1)\frac{\Delta_n}{\delta_n}\exp\left(-\frac{\Delta_n}{\delta_n}\right) \text{for } \Delta_n \le 0, \\ T_{t,a}(\Delta_n, \Delta_t) &= T_{t,\max}\sqrt{2\exp(1)}\ \frac{\Delta_t}{\delta_t}\exp\left(-\frac{\Delta_n}{\delta_n}\right)\exp\left(-\frac{\Delta_t^2}{\delta_t^2}\right), \end{aligned} \tag{13}$$

where Δ_n and $\Delta_t = \sqrt{\Delta_1^2 + \Delta_2^2}$ represent the displacement discontinuities at the interface in the normal and tangential directions, respectively. And $T_{n,\max}$ and $T_{t,\max}$ are the maximum normal and tangential tractions with $\Delta_t = 0$ and $\Delta_n = 0$, respectively; and δ_n and δ_t are parameters corresponding to the peak stress.

The adhesive normal traction T_n and tangential traction $T_{t,a}$, respectively, reach their maximum values $T_{n,\max}$ and $T_{t,\max}$ at the jumps of δ_n and $(\delta_t/\sqrt{2})$. The δ_n and δ_t are determined through the fracture energy of the interface G_s, as follows:

$$\delta_n = \frac{G_s}{T_{n,\max} \exp(1)},$$
$$\delta_t = \frac{G_s}{T_{t,\max} \sqrt{0.5 \exp(1)}}. \tag{14}$$

The frictional force is coupled to the adhesive force through the damage variable at the interface d_s, as follows:

$$T_{t,f} = \frac{1}{1 - d_s^{0.1}} \cdot \mu_f \cdot |T_n| \text{for } \Delta_n \le 0, \tag{15}$$

where μ_f is the frictional coefficient. It is highlighted that the $d_s^{(1-d_s^{0.1})}$ in equation (15) is used to replace the conventional d_s in the following equation [28–30]:

$$T_{t,f} = d_s \cdot \mu_f \cdot |T_n| \text{for } \Delta_n \le 0. \tag{16}$$

The damage variable at the interface d_s is expressed as follows:

$$d_s = \max\{d_{s,n}, d_{s,t}\} = \max\left\{1 - \exp\left(-\frac{\kappa_n}{\delta_n}\right), 1 - \exp\left(-\frac{\kappa_t^2}{\delta_t^2}\right)\right\}, \tag{17}$$

where κ_n and κ_t denote the maximum normal and tangential jumps ever attained.

Equation (15) is preferable to equation (16) as it agrees well with the slant shear test results, where the measured bond strength is the sum of the adhesion and friction components, as shown in Figure 6.

3.5. Implementation in Abaqus/Standard. Due to the powerful implicit solver and automated time-stepping procedures, Abaqus/Standard was selected. Additionally, the user-defined element (UEL) subroutine was utilized to characterize the cohesive element's kinematic relationship and the coupled adhesive-frictional relationship at the interface.

When employing the UEL subroutine, the important arrays required are the tangent stiffness matrix and the right-hand-side residual vector, namely, AMATRX and RHS, respectively. It is noted that our previous work [31] presents detailed expressions for the quadrilateral 4-noded cohesive element (2D). The extension to the 8-noded cohesive element (3D) is straightforward. The source code (UEL) for the 2D case can be found at https://pan.baidu.com/s/1Fuctc9JJwnAmWGEtTke1OA (password: z4fn). And later, the 3D case would also be released at the same repository.

4. Analytical Model

The failure patterns indicate that the following mechanisms should be accounted for to accurately give the analytical solution for uniaxial stress-strain behavior (see Figure 7): (1) confinement effect, of which the UHPC shell confines the lateral deformation of the core concrete; (2) indirect load-carrying effect, of which the UHPC would also sustain the uniaxial load partially, transferred from the tangential traction at the UHPC-NC interface; and (3) interfacial debonding, of which first identified in our square and rectangular specimen, and it would affect the load transferred to the UHPC shell.

4.1. Circular Specimen

4.1.1. Confining Pressure. It is assumed that for circular specimens, the confining pressure $\sigma_{I,r}$ from the UHPC shell distributes uniformly along the circumference. Therewith, the $\sigma_{I,r}$ for circular ones is obtained as follows:

$$\sigma_{I,r} = \frac{\sigma_{E,\theta}(r_E - r_I)}{r_I}, \tag{18}$$

where r_E and r_I are the external and internal radii, respectively, and $\sigma_{E,\theta}$ is the tensile stress inside the UHPC shell (see Figure 7). The tensile stress $\sigma_{E,\theta}$ is strongly correlated with the hoop strain of the UHPC $\varepsilon_{E,\theta}$ along the circumference, and it is taken as $\sigma_{E,\theta} = E_E \cdot \varepsilon_{E,\theta} \le f_{c,E}$ ($E_E = 55.5$ GPa and $f_{c,E} = 5.5$ MPa for UHPC) before cracking and $\sigma_{E,\theta} = 0.8 f_{c,E}$ after cracking, as shown in Figure 3.

Treating the UHPC shell as a thick wall, we can relate the strain of the UHPC along the circumstance $\varepsilon_{E,\theta}$ to the hoop strain of the core concrete $\varepsilon_{I,r}$, as [16] follows:

$$\varepsilon_{E,\theta} = \varepsilon_{I,r} \frac{(1 - 2\nu) + (r_E/r_I)}{(1 - 2\nu) + (r_E/r_I)^2}, \tag{19}$$

with $\nu = 0.2$, Poisson's coefficient of UHPC.

4.1.2. Hoop-Vertical Strain Relationship. Teng et al. [32] proposed a prediction equation to describe the relationship between the hoop and axial strain ($\varepsilon_{I,r}$ and ε_z) as follows:

$$\varepsilon_z = 0.85\left(\alpha + \beta \frac{\sigma_{I,r}}{f_{co}'}\right)\left\{\left[1 + 0.75\left(\frac{\varepsilon_{I,r}}{\varepsilon_{co}}\right)\right]^{0.7} - \exp\left[-7\left(\frac{\varepsilon_{I,r}}{\varepsilon_{co}}\right)\right]\right\}, \tag{20}$$

where f_{co}' and ε_{co} denote the compressive strength and the correspond strain of unconfined concrete, respectively; $\sigma_{I,r}$ represents the confining pressure on the core concrete; and α and β are empirical constants. Reference [16] recommended $\alpha = 1$ and $\beta = 2$ for the core concrete confined by the UHPC shell.

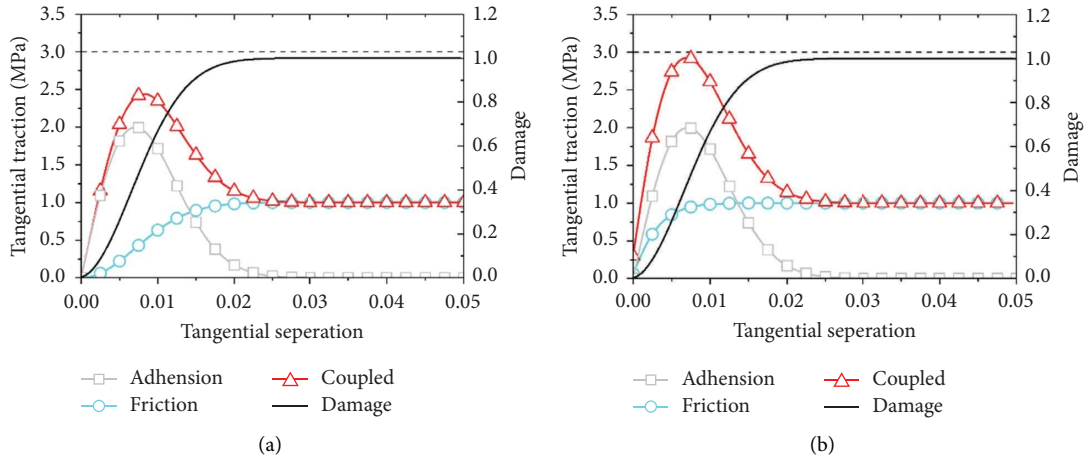

Figure 6: Illustration of the conventional and proposed coupled adhesive-frictional model. (a) Conventional (equation (18)). (b) Proposed (equation (17)).

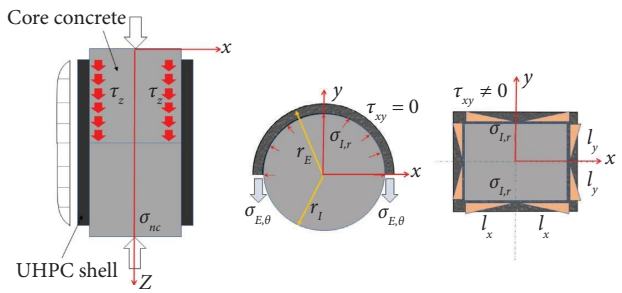

Figure 7: Load transfer of the core concrete-confined UHPC shell.

4.1.3. Active-Confinement Model. Compressive strength of confined core concrete f_{cc}' and the corresponding peak strain ε_{cc} are given by [32, 33], respectively, as follows:

$$f_{cc}' = f_{co}' + 3.5\sigma_{I,\theta},$$
$$\varepsilon_{cc} = \varepsilon_{co} + 5\varepsilon_{co}\left(\frac{f_{cc}'}{f_{co}'} - 1\right). \tag{21}$$

Popovics [34] provided the compressive stress-strain curve for confined core concrete, which is as follows:

$$\sigma_{c,1} = \frac{(\varepsilon_c/\varepsilon_{cc})r}{r - 1 + (\varepsilon_c/\varepsilon_{cc})^r} f_{cc}',$$
$$r = \frac{E_c}{E_c - (f_{cc}'/\varepsilon_{cc})}, \tag{22}$$

where $\sigma_{c,1}$ and ε_c denote the axial compressive stress and corresponding axial strain of confined concrete, respectively; E_c represents the elastic modulus of normal concrete.

4.1.4. Vertical Load by the UHPC Shell. Although the height of the core concrete is 20 mm longer than the UHPC shell (see Figure 1), the shell also sustains part of the external compressive force, due to the tangential stress τ_z along the interface. The equation to calculate the uniaxial compressive stress sustained by the UHPC shell is as follows:

$$\sigma_{c,2} = \begin{cases} E_u\varepsilon_z \text{ before debonding,} \\ \mu \cdot \sigma_{I,r} \cdot \dfrac{r_I \cdot h}{\pi\left(r_E^2 - r_I^2\right)} \text{ after debonding,} \end{cases} \tag{23}$$

where μ is the frictional coefficient between UHPC and NC materials, and h represents the height of the UHPC shell.

For circular specimens, the tangential traction along the circumstance does not exist $\tau_{xy} = 0$, and we only need to consider τ_z. Before debonding, the fore equilibrium requires that

$$\tau_z = 2\frac{E_u\varepsilon_z \cdot \pi\left(r_E^2 - r_I^2\right)}{r_I \cdot h} \text{ before debonding.} \tag{24}$$

From the slant shear test, if the tangential traction $\tau_z \le (c + \mu \cdot \sigma_{I,\theta})$, the UHPC-NC interface remains overall integrity without debonding. However, if debonding occurs, the adhesive force vanishes and tangential traction τ_z is only related to the frictional force, as follows:

$$\tau_z = \mu \cdot \sigma_{I,\theta} \text{ after debonding.} \tag{25}$$

With the uniaxial compressive stress inside the confined core concrete $\sigma_{c,1}$ and the UHPC shell $\sigma_{c,2}$, the overall uniaxial stress σ_c corresponding to the given uniaxial strain ε_z is given as follows:

$$\sigma_c = \frac{\sigma_{c,1}r_I^2 + \sigma_{c,2}\left(r_E^2 - r_I^2\right)}{r_I^2}. \tag{26}$$

4.1.5. Step-by-Step Procedure. The strep-by-step procedure to determine the uniaxial stress-strain constitutive law for UHPC shell-confined core concrete is given as follows:

Step 1: given an axial strain ε_z, assuming the confining pressure $\sigma_{I,r}$;

Step 2: calculate the corresponding hoop strain $\varepsilon_{I,r}$;

Step 3: calculating the strain within the UHPC shell $\varepsilon_{E,\theta}$;

Step 4: evaluate the stress inside the UHPC shell $\sigma_{E,\theta}$ as per the tensile constitutive law;

Step 5: calculate the confining pressure $\sigma_{I,r}$;

Step 6: compare the $\sigma_{I,r}$ in Set 5 and the assumed one in Step 1. If the difference exceeds the acceptable tolerance, return to Step 1;

Step 7: substitute the axial strain ε_z and converged confining pressure $\sigma_{I,r}$ into the active-confinement model and obtain the corresponding uniaxial stress inside core concrete $\sigma_{c,1}$;

Step 8: judge the debonding of interface, and calculate the uniaxial stress inside the UHPC shell $\sigma_{c,2}$;

Step 9: obtain the overall uniaxial stress σ_c.

4.2. Square and Rectangular Specimen

4.2.1. Confining Pressure. The confining pressure σ_r in square and rectangular specimens is unevenly distributed, leading to uneven confinement of the core concrete. Relying on the plane strain condition and Airy's function, the confining pressure is given as follows and also illustrated in Figure 7.

$$\begin{aligned}\sigma_{I,\theta x} &= \frac{1}{2}\left(A_x + A_y\right)x^2 - A_y y^2 - B_x\left(l_x\right)^2,\\ \sigma_{I,\theta y} &= \frac{1}{2}\left(A_x + A_y\right)y^2 - A_x x^2 - B_y\left(l_y\right)^2,\\ \tau_{I,\theta xy} &= -\left(A_x + A_y\right)xy,\end{aligned} \tag{27}$$

where l_x and l_y denote half of the length and width of the specimen, respectively, with $l_x \geq l_y$; A_x, A_y, B_x, and B_y are four Airy's constants that can be derived by minimizing the difference between the total displacement of the UHPC shell and core concrete. Specific expressions for these constants are provided in Appendix A.

The tensile stress along the x and y directions ($\sigma_{E,\theta x}$ and $\sigma_{E,\theta y}$) of the UHPC shell can be obtained as follows:

$$\begin{aligned}\sigma_{E,rx} &= \frac{l_y}{3\left(r_E - r_I\right)}\left(3B_x l_x^2 + A_x l_y^2\right),\\ \sigma_{E,ry} &= \frac{l_x}{3\left(r_E - r_I\right)}\left(3B_y l_y^2 + A_y l_x^2\right).\end{aligned} \tag{28}$$

Similarly, the tensile stress $\sigma_{E,\theta} = \max\left\{\sigma_{E,\theta x}, \sigma_{E,\theta y}\right\}$ is taken as $\sigma_{E,r} = E_E \cdot \varepsilon_{E,r} \leq f_{c,E}$ ($E_E = 55.5\,\text{GPa}$ and $f_{c,E} = 5.5\,\text{MPa}$ for UHPC) before cracking and $\sigma_{E,r} = 0.8 f_{c,E}$ after cracking.

The equivalent confining pressure $\overline{\sigma}_{I,r}$ is adopted, and it could reflect the global behavior of the confined core concrete, as [35] follows:

$$\overline{\sigma}_{I,r} = \frac{\left(l_x - l_y\right)^2}{12}\left(A_y - A_x\right)x^2 - \frac{1}{2}\left(B_x l_x^2 + B_y l_y^2\right). \tag{29}$$

It is noted that equations (28) and (29) degenerate for the square specimen with $l_x = l_y$.

4.2.2. Hoop-Vertical Strain Relationship. Different from the specimens with a circular cross section, where the empirical hoop-vertical strain relationship is employed, equations (28)~(29) directly relate the confining pressure $\overline{\sigma}_{I,r}$ to the vertical strain ε_z, and it does not require the hoop-vertical strain relationship.

4.2.3. Active-Confinement Model. The active-confinement mode is identical to the one in Section 4.1.

4.2.4. Vertical Load by the UHPC Shell. The calculation of the vertical load sustained by the UHPC shell is identical to that of the circular specimen, except the determination of interfacial debonding. For square and rectangular specimens, the tangential traction along the circumstance τ_{xy} is not zero, and the overall tangential stress τ is as follows:

$$\tau = \sqrt{\tau_z^2 + \tau_{xy}^2}\ \text{before debonding}, \tag{30}$$

where $\tau_{xy} = \tau_{I,\theta xy}$ is determined by equation (28). Subsequently, the tangential stress τ is employed to determine the occurrence of the interfacial debonding.

4.2.5. Step-by-Step Procedure. The strep-by-step procedure to determine the uniaxial stress-strain constitutive law for UHPC shell-confined core concrete is given as follows:

Step 1: given an axial strain ε_z;

Step 2: evaluate Airy's constant A_x, A_y, B_x, and B_y;

Step 3: calculate the tensile stress in the UHPC shell $\sigma_{E,r}$;

Step 4: obtain the equivalent hoop stress $\overline{\sigma}_{I,r}$;

Step 5: substitute the axial strain ε_z and converged confining pressure $\overline{\sigma}_{I,r}$ into the active-confinement model and obtain the corresponding uniaxial stress inside core concrete $\sigma_{c,1}$;

Step 6: evaluate the tangential tractions τ_{xy} and τ_z and therewith τ;

Step 7: judge the debonding of the interface, and calculate the uniaxial stress inside the UHPC shell $\sigma_{c,2}$;

Step 8: obtain the overall uniaxial stress σ_c.

5. Experimental Results and Discussions

5.1. Failure Patterns. The concrete columns, without UHPC shells, failed suddenly with explosive sound. Concrete crushing of specimens, CU-C50 and SU-C50, was observed, with main vertical cracks evolved along their axes (see Figure 8(a)).

Various failure modes were detected in the specimens wrapped with the UHPC shell. As opposed to concrete crushing, the fracture of the UHPC shell was the defining characteristic of columns confined by UHPC. The damage

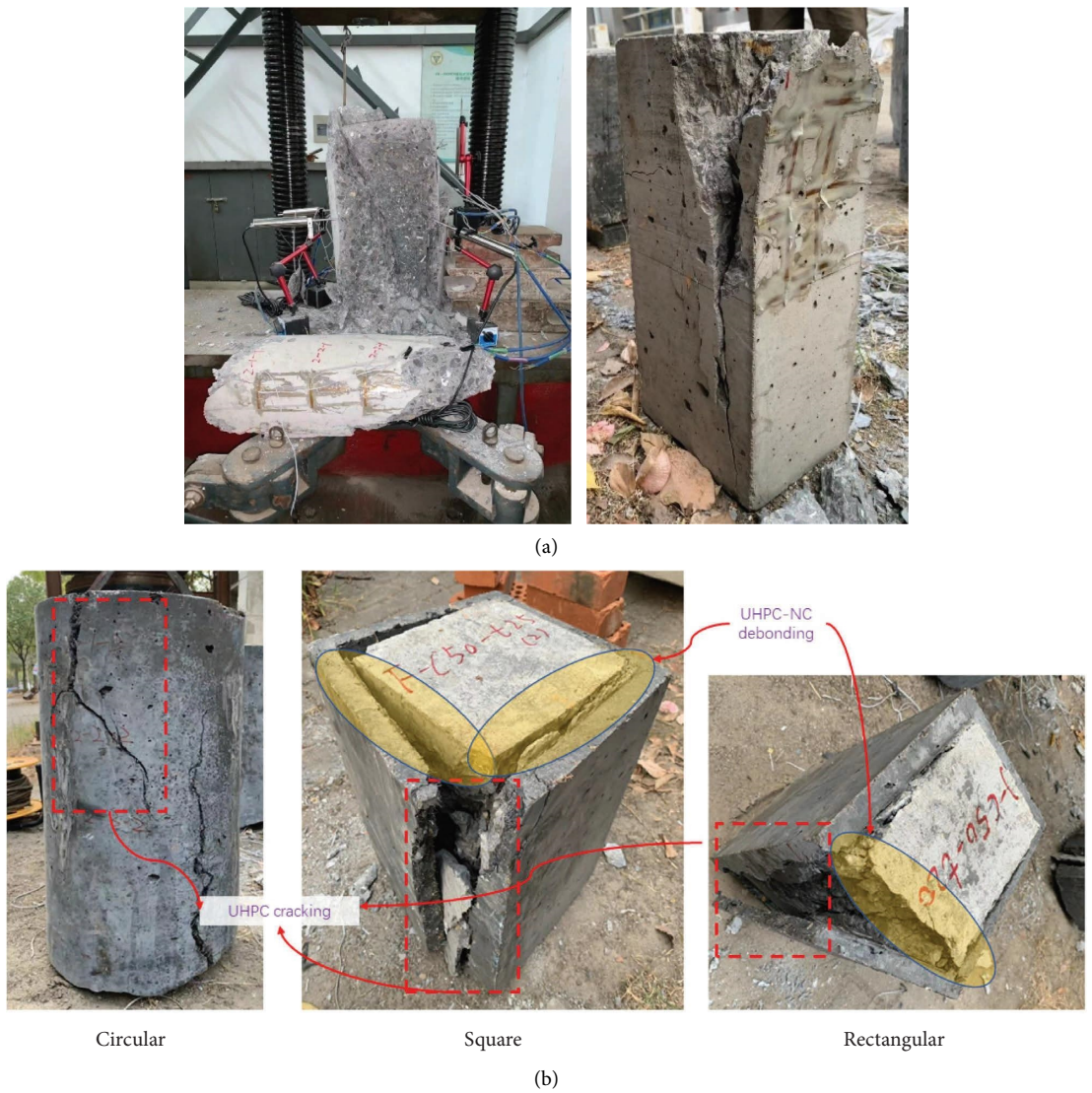

Figure 8: Failure patterns. (a) Unconfined concrete. (b) Core concrete confined by the UHPC shell.

evolution of the specimen CC-C50-U25 was presented in Figure 8(b). When the external load was applied to 1200 kN, spalling of the inner concrete column at the two ends was witnessed. However, the load capacity was able to be continually increased until the minor cracking of the UHPC shell took place at an external force of 1700 kN. The results showed that the presence of cracks in the UHPC matrix did not cause immediate specimen failure. Instead, the steel fibers induced crack bridging, allowing for the external load to increase to 2800 kN, which was accompanied by the main crack inside the UHPC shell.

Similar damage evolutions could be found in square and rectangular specimens, as shown in Figure 8(b) for the specimen SC-C50-U25. However, a significant debonding was observed between the UHPC shell and the core NC column at the point of failure. The debonding was identified in the rectangular and square specimens but not the circular ones.

Table 1 gives the measured the peak stress f'^{*}_{cc} and corresponding strain ε'^{*}_{cc} for tested specimens. Initially, we concentrate on the impact of UHPC shell thickness on the uniaxial behavior of the specimens. In comparison to the unconfined specimen RU-C50, the peak stress f'^{*}_{cc} of specimens, RC-C50-U15, RC-C50-U20 and RC-C50-U25, was increased by 10.0%, 19.0%, and 27.0%, respectively. However, the corresponding peak strain ε'^{*}_{cc} showed a significant increase of more than 70%.

The enhancement of the UHPC shell on the core concrete with different compressive strength f'^{*}_{co} is then investigated. Table 1 suggested that the enhancement of the peak stress f'^{*}_{cc} was more apparent for a UHPC-confined specimen with a lower core concrete strength (specimens RC-C50-U20 and RC-C30-U20, and specimens RC-C50-U15 and RC-C30-U15). The experimental results agreed with other researchers [16]. However, the difference in the corresponding peak strain ε'^{*}_{cc} is not apparent.

Furthermore, Table 1 also suggested that the UHPC shell is more effective in enhancing circular specimens, rather than square or rectangular specimens. Specifically, the peak stress f'^{*}_{cc} was enhanced by 50.0% for C-50-25, 40% for S-50-25, and only 27% for R-50-25. Comparatively, the enhancement of the peak strain ε'^{*}_{cc} was similar.

The experimental normalized stress-strain relations for the tested specimens are also presented in Figure 9. It is noted that postpeak behaviors were missing due to the force-controlled loading scheme. It is apparently true that for unconfined specimens, the behavior was quite brittle due to the smaller failure strain. However, for UHPC-confined specimens, apparent nonlinear ascending branches were witnessed after the cracking of the UHPC shell. The utilization of the UHPC shell resulted in a significant increase in both the peak stress f'^{*}_{cc} and peak strain ε'^{*}_{cc}.

5.2. Numerical Results. The maximum strain (LE) contour observed in the circular specimen (CC-C50-U25), the square specimen (SC-C50-U25), and the rectangular specimen (RC-C50-U25) at failure are comparatively plotted with experimental photos with main cracks in Figure 10. Two numerical results are presented: one labeled "*coupled adhesive-frictional model*" and the other labeled "perfect bond." It shows that the proposed model integrating the CDP model and coupled adhesive-friction mode well predicts the cracks that evolved in the UHPC shell and the failure patterns. However, the assumption of "perfect bonding" between UHPC and NC, which ignores tangential sliding, results in a poor crack pattern.

This indicates that the tensile stresses are highly concentrated at the midpoint of circular specimens and inside corners of square and rectangular specimens. The cracks in the numerical simulations therewith form at the midspan and extend toward the corners. However, this phenomenon contradicts with the experimental phenomenon that the real cracks were activated at the corner and propagated toward the midspan. A similar phenomenon was reported by Ronanki and Aaleti [3], who attributed it to insufficient fiber distribution at the corners, which resulted in lower tensile strength of the UHPC shell at two ends. However, the discrepancy in the evolution of cracks does not impact the numerical normalized stress-strain curves.

Experimental and numerical normalized stress-strain curves are compared in Figure 11, which indicates that the initial stiffness, peak stress, and corresponding strain are captured in an agreed manner. It indicates that all the simulation curves are within the scope of ±10% errors for tested specimens.

Specimens, SC-C50-U25 and RC-C50-U25, which have the perfect UHPC-NC bond, are deliberatively selected to illustrate the role of UHPC-NC interfacial debonding in the confining effect of the UHPC shell. It is highlighted that the perfect bond would overestimate the stress. Therefore, for square and rectangular specimens, it is critical to realistically consider the UHPC-NC interfacial response, of which the tangential traction is not evenly distributed, and the bond failure would occur.

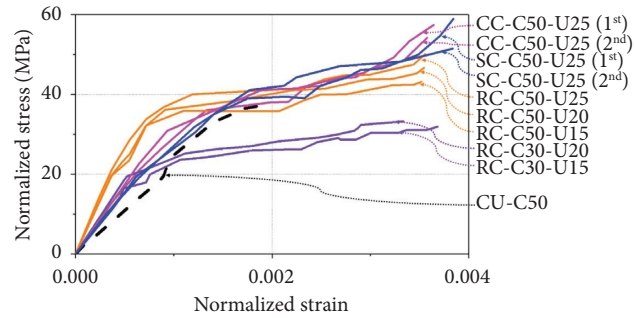

Figure 9: Experimental normalized stress-strain curves.

5.3. Experimental and Analytical Solutions. With the analytical solution in Sect. 4, the analytical normalized stress-strain curves of selected tested specimens are comparatively plotted in Figure 12.

Figure 12(a) shows the circular specimen confined by the UHPC shell (specimen CC-C50-U25). The cracking of the UHPC shell is numerically predicted at the uniaxial stress of 40.4 MPa, which is acceptable compared to the experimental values of 36.1 MPa. The predicted peak stress is $f'^{*}_{cc} = 55.8$ MPa, which also approaches the experimental values of $f'^{*}_{cc} = 57.1$ MPa and 54.0 MPa.

Similarly, the predicted normalized stress-strain curve of square specimens is also compared in Figure 12(b), along with the UHPC shell's cracking point. For the specimen, RC-C50-U25, the predicted cracking stress is 44.6 MPa, which is also comparable to experimental ones, 38.2 MPa and 39.3 MPa. The difference in the analytical and experimental peak stress and strain is also acceptable with the maximum of 12% difference.

The normalized stress-strain curves of rectangular specimens show more apparent plateau branches after the cracking of the UHPC shell (see Figures 12(c) and 12(d)). The reason is that the debonding of the UHPC-NC interface occurred and the UHPC shell could not sustain the vertical load anymore. This phenomenon is also predicted by the analytical model, together with the cracking and peak point.

Figure 13 presents a comparison between the analytical vertical strain of the UHPC shell and experimental values. Regarding the circular specimen, the vertical strain of the UHPC shell shows a nearly linear increase with overall uniaxial strain ε_z, suggesting that the UHPC-NC interface demonstrated good performance, and there was no occurrence of debonding. However, the vertical strain of the UHPC shell reached its plateau soon. Meanwhile, interfacial debonding was witnessed in these specimens. The proposed analytical mode can capture the debonding behavior. However, some discrepancies were noted, which may be attributed to the progressive evolution of debonding observed in the tests, whereas the analytical model assumes simultaneous failure of the entire interface.

6. Summary and Final Remarks

This study utilized experimental, numerical, and analytical methods to examine the behavior of core concrete subjected to uniaxial compression and confined by UHPC shells. From the results obtained, several conclusions were drawn as follows:

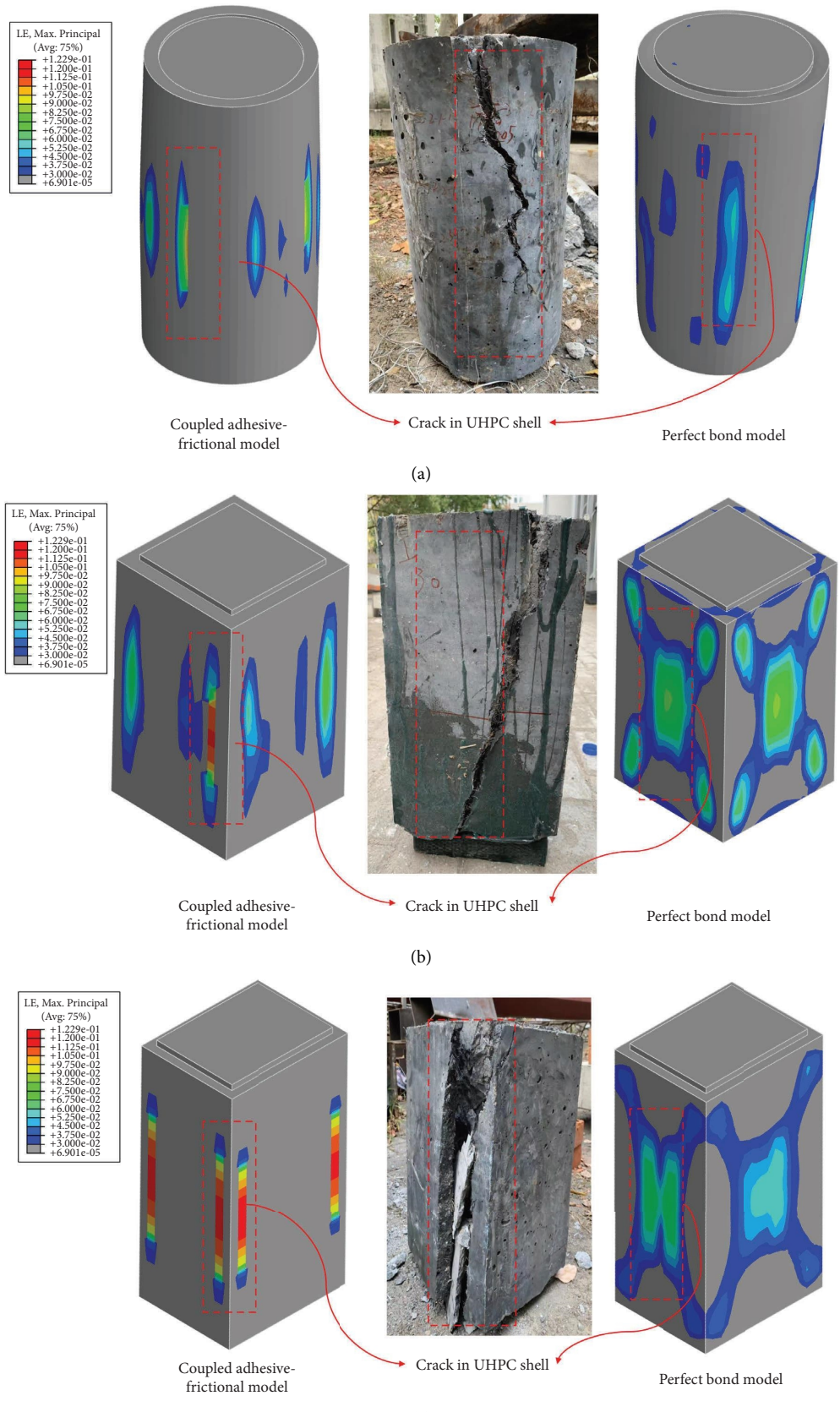

Figure 10: The FE predicted failure pattern vs. experimental ones. (a) Specimen CC-C50-U25. (b) Specimen SC-C50-U25. (c) Specimen RC-C50-U25.

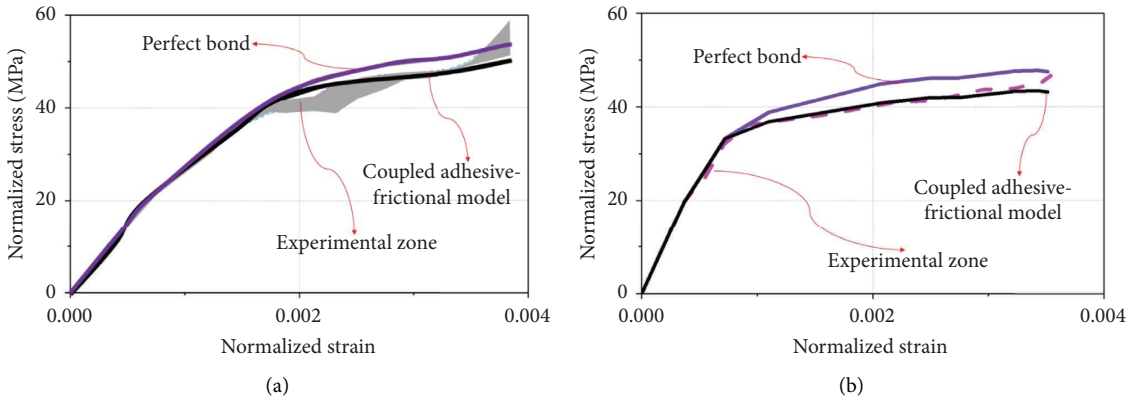

Figure 11: Comparison of the numerical and experimental normalized stress-strain model with the coupled adhesive-frictional model and perfect bond. (a) Specimen SC-C50-U25. (b) Specimen RC-C50-U20.

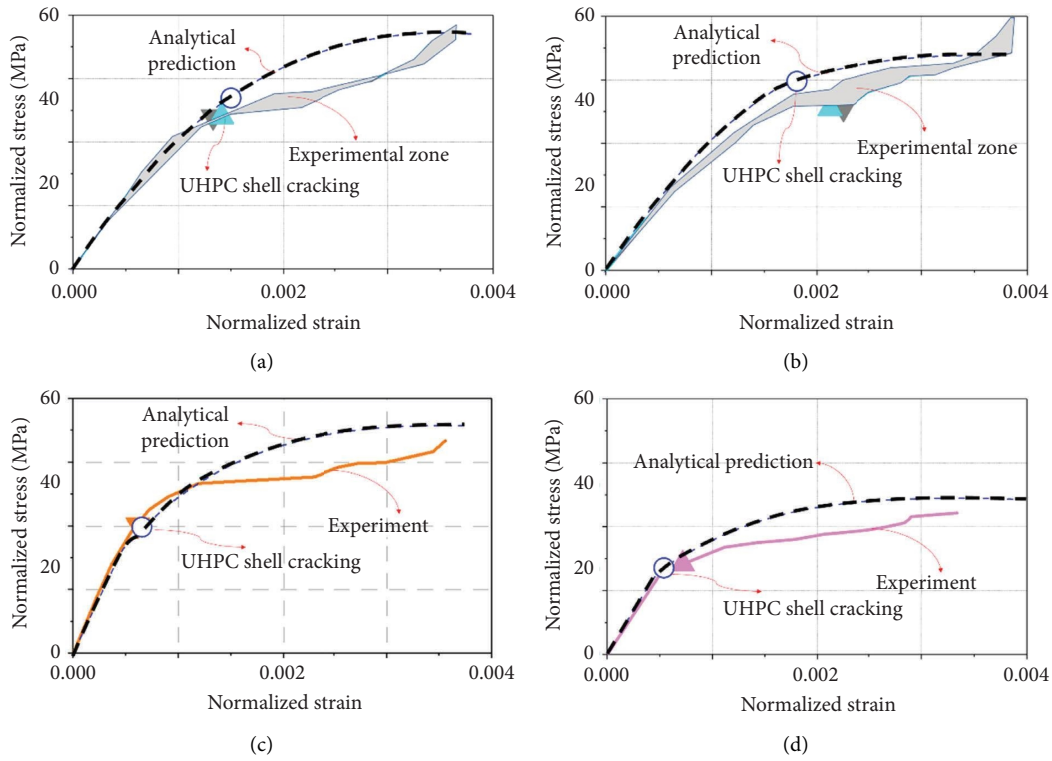

Figure 12: Experimental normalized stress-strain curves. (a) Specimen CC-C50-U25. (b) Specimen RC-C50-U25. (c) Specimen SC-C50-U25. (d) Specimen SC-C30-U20.

(1) The UHPC shell significantly improved the peak stress and corresponding strain of the circular-shaped core concrete specimens with lower compressive strength. However, the confinement of the UHPC shell on the rectangular specimens was the least effective.

(2) The UHPC shell altered the failure pattern of the core concrete. The cracking of the UHPC shell replaced conventional crushing. More importantly, the UHPC-NC debonding was identified in square or rectangular specimens.

(3) In order to model the interfacial behavior, the coupled adhesive-frictional model is implemented in the cohesive element, which is realized through the UEL subroutine in Abaqus/Standard. It is validated that interfacial behavior is essential to capture the cracking evolution and stress-strain relation accurately.

(4) An analytical solution is derived for the uniaxial stress-strain relationship of core concrete confined by the UHPC shell, taking into account factors such as confinement, interfacial debonding, and vertical

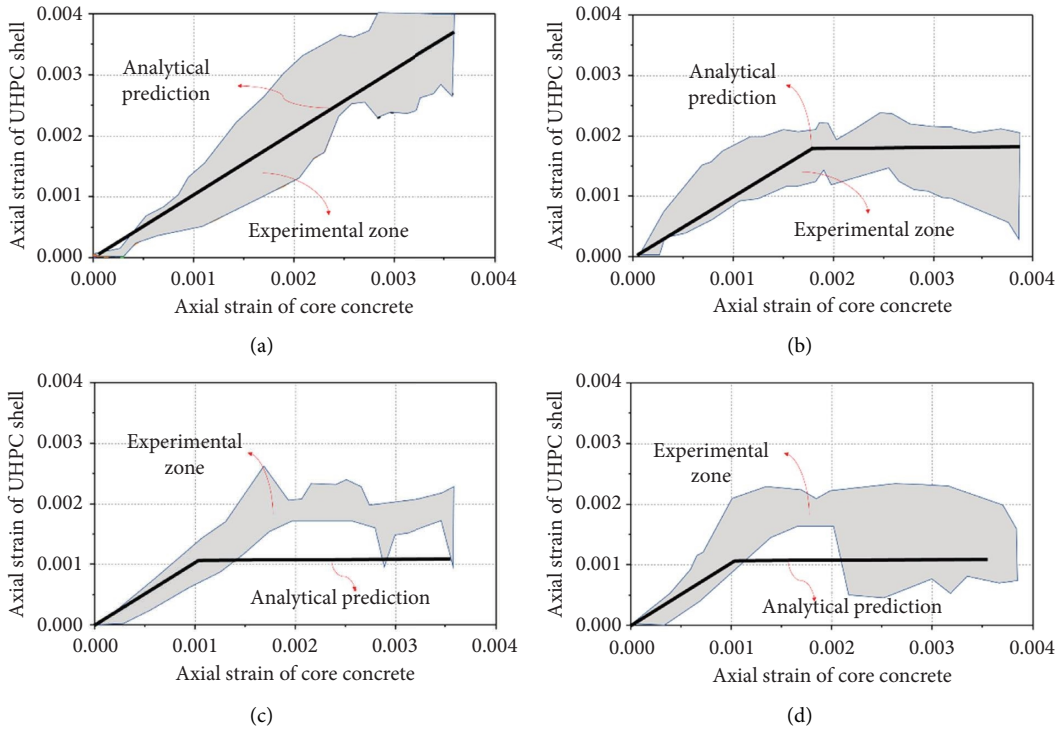

Figure 13: Comparison of experimental and analytical prediction of vertical strain in the UHPC shell and core concrete. (a) Specimen CC-C50-U25. (b) Specimen RC-C50-U25. (c) Specimen SC-C50-U25. (d) Specimen SC-C30-U20.

load sustained by the UHPC shell. The solution accurately predicts the compressive capacity of the tested specimens.

The study experimentally exhibited that the uniaxial behavior of core concrete confined by the UHPC shell is completed, especially when the debonding of the interface was involved. However, the quantity of the specimens is rather limited, and further experiments are needed to validate the confinement impact of the UHPC shell.

Appendix

A_x, A_y, B_x, and B_y are determined by minimizing the discrepancy between the total displacement of the UHPC shell and the concrete column. The detailed derivation can be found in Tong et al. [31]. The constants A_x and A_y are as follows:

$$A_x = \frac{42(E_c)^2 E_E t\nu}{D_{Ax}}\left[E_c l_x l_y N_{Ax,1} - 12E_E t(1+\nu)N_{Ax,2}\right]\varepsilon_z,$$

$$A_y = \frac{42(E_c)^2 E_E t\nu}{D_{Ay}}\left[E_c l_x l_y N_{Ay,1} - 12E_E t(1+\nu)N_{Ay,2}\right]\varepsilon_z, \tag{A.1}$$

where

$$\begin{aligned}
N_{Ax,1} &= E_c l_x (l_y)^2 \left(21 l_x l_x - 21 l_x l_y + 8 l_y l_y\right),\\
N_{Ax,2} &= E_c (l_x)^2 (l_y)^2 \left(7 l_x l_x - 13 l_y l_y\right),\\
N_{Ay,1} &= E_c l_y (l_x)^2 \left(21 l_y l_y - 21 l_x l_y + 8 l_x l_x\right),\\
N_{Ay,2} &= E_c (l_x)^2 (l_y)^2 \left(7 l_y l_y - 13 l_x l_x\right),\\
D_{Ax} &= D_{Ay},
\end{aligned} \tag{A.2}$$

with

$$\begin{aligned}
D_{Ax} &= 532(E_E)^2 t^2 (1+\nu)\left(E_c l_x l_y\right)^2 D_{Ax,1}\\
&\quad + 12E_E t E_c l_x l_y \left(E_c l_x l_y\right)^2 D_{Ax,4} + 2(E_c)^2 l_x l_y D_{Ax,7},\\
D_{Ax,1} &= 7\nu l_x^4 + 2 l_x^2 l_y^2 (10 - 3\nu) + 7\nu l_y^4,\\
D_{Ax,4} &= 63 l_x^3 + 13 l_x^2 l_y (4 + 7\nu) + 13 l_x l_y^2 (4 + 7\nu) + 63 l_y^3,\\
D_{Ax,7} &= 2E_c^2 l_x^2 l_y^2 \left(21 l_x^4 + 8 l_x^2 l_y^2 + 21 l_y^2\right).
\end{aligned} \tag{A.3}$$

Further, the constants B_x and B_y are as follows:

$$B_x = \frac{6E_c E_E t\nu}{D_{Bx}}\left[12E_E t(1+\nu)N_{Bx,1} - 12(E_c)^3 (l_x)^3 (l_y)^2 N_{Bx,2}\right]\varepsilon_z,$$

$$B_y = \frac{6E_c E_E t\nu}{D_{By}}\left[12E_E t(1+\nu)N_{By,1} - 12(E_c)^3 (l_y)^3 (l_x)^2 N_{By,2}\right]\varepsilon_z, \tag{A.4}$$

where

$$D_{Bx} = (l_x)^2 D_{Ax},$$
$$D_{By} = (l_y)^2 D_{Ay},$$
$$N_{Bx,1} = (E_c)^2 (l_x)^2 (l_y)^2 \left(21 (l_x)^4 + 8 (l_x)^2 (l_y)^2 + 7 (l_y)^4\right),$$
$$N_{Bx,2} = 28 (l_x)^4 - 8 (l_x)^2 (l_y)^2 + 49 l_x (l_y)^3 - 21 (l_y)^4,$$
$$N_{By,1} = (E_c)^2 (l_x)^2 (l_y)^2 \left(21 (l_y)^4 + 8 (l_x)^2 (l_y)^2 + 7 (l_x)^4\right),$$
$$N_{By,2} = 28 (l_y)^4 - 8 (l_x)^2 (l_y)^2 + 49 l_y (l_x)^3 - 21 (l_x)^4. \quad (A.5)$$

Poisson's ratio of concrete ν is related to the uniaxial strain ε_z, as [36] follows:

$$\nu(\varepsilon_z) = \nu_0 \left[1 + 0.2\left(\frac{\varepsilon_z}{\varepsilon_{co}}\right) - \left(\frac{\varepsilon_z}{\varepsilon_{co}}\right)^2 + 1.55\left(\frac{\varepsilon_z}{\varepsilon_{co}}\right)^3\right] \leq 0.5, \quad (A.6)$$

where $\nu_0 = 0.2$ and ε_{co} is the strain at stress peak of the unconfined concrete.

Data Availability

The datasets generated during and/or analysed during the current study are available from the corresponding author on reasonable request.

Additional Points

Highlights. (i) The UHPC shell alters the failure pattern of confined core concrete. (ii) We integrate the CDP model for the matrix and the coupled adhesive-frictional model for the UHPC-NC interface. (iii) We propose analytical solution for uniaxial stress-strain relationship of the UHPC-confined core concrete.

Disclosure

The funder was not involved in the study design, collection, analysis, interpretation of data, the writing of this article, or the decision to submit it for publication.

Conflicts of Interest

The authors declare that there are no conflicts of interest.

Acknowledgments

This research was supported by the independent science and technology project (W22FZ2730013) of State Grid Gansu Electric Power Engineering Consulting Co., Ltd., Lanzhou.

References

[1] T. Tong, S. Yuan, W. Zhuo, Z. He, and Z. Liu, "Seismic retrofitting of rectangular bridge piers using ultra-high performance fiber reinforced concrete jackets," *Composite Structures*, vol. 228, Article ID 111367, 2019.

[2] T. Tong, J. Wang, H. Lei, and Z. Liu, "UHPC jacket retrofitting of reinforced concrete bridge piers with low flexural reinforcement ratios: experimental investigation and three-dimensional finite element modeling," *Structure and Infrastructure Engineering*, vol. 17, no. 10, pp. 1315–1337, 2021.

[3] V. S. Ronanki and S. Aaleti, "Experimental and analytical investigation of UHPC confined concrete behavior," *Construction and Building Materials*, vol. 325, Article ID 126710, 2022.

[4] X. Nie, Y. Yang, J. Fan, Y. L. Mo, and J. Nie, "Experimental study on steel jacket–concrete composite connections," *Journal of Bridge Engineering*, vol. 22, no. 4, Article ID 4016138, 2017.

[5] M. Ding, X. Chen, X. Zhang, Z. Liu, and J. Lu, "Study on seismic strengthening of railway bridge pier with CFRP and concrete jackets," *Earthquakes and Structures*, vol. 15, no. 3, pp. 275–283, 2018.

[6] S. Cabral-Fonseca, J. R. Correia, J. Custódio, H. M. Silva, A. M. Machado, and J. Sousa, "Durability of FRP-concrete bonded joints in structural rehabilitation: a review," *International Journal of Adhesion and Adhesives*, vol. 83, pp. 153–167, 2018.

[7] Z. Yu, L. Wu, Z. Yuan, C. Zhang, and T. Bangi, "RETRACTED: mechanical properties, durability and application of ultra-high-performance concrete containing coarse aggregate (UHPC-CA): a review," *Construction and Building Materials*, vol. 334, Article ID 127360, 2022.

[8] S. Deng, X. Shao, X. Zhao, Y. Wang, and Y. Wang, "Precast steel—UHPC lightweight composite bridge for accelerated bridge construction," *Frontiers of Structural and Civil Engineering*, vol. 15, no. 2, pp. 364–377, 2021.

[9] C. C. Hung, H. S. Lee, and S. N. Chan, "Tension-stiffening effect in steel-reinforced UHPC composites: constitutive model and effects of steel fibers, loading patterns, and rebar sizes," *Composites Part B: Engineering*, vol. 158, pp. 269–278, 2019.

[10] S. Ghasemi, A. Mirmiran, Y. Xiao, and K. Mackie, "Novel UHPC-CFRP waffle deck panel system for accelerated bridge construction," *Journal of Composites for Construction*, vol. 20, no. 1, Article ID 4015042, 2016.

[11] T. Tong, H. Lei, S. Yuan, and Z. Liu, "Experimental investigation and seismic vulnerability assessment of low flexural strength rectangular bridge piers retrofitted with ultrahigh-performance concrete jackets," *Engineering Structures*, vol. 206, Article ID 110132, 2020.

[12] M. A. Dagenais, B. Massicotte, and G. Boucher-Proulx, "Seismic retrofitting of rectangular bridge piers with deficient lap splices using ultrahigh-performance fiber-reinforced concrete," *Journal of Bridge Engineering*, vol. 23, no. 2, Article ID 4017129, 2018.

[13] M. Farzad, A. Sadeghnejad, S. Rastkar, A. Moshkforoush, and A. Azizinamini, "A theoretical analysis of mechanical and durability enhancement of circular reinforced concrete columns repaired with UHPC," *Engineering Structures*, vol. 209, Article ID 109928, 2020.

[14] S. Xu, C. Wu, Z. Liu et al., "Experimental investigation of seismic behavior of ultra-high performance steel fiber reinforced concrete columns," *Engineering Structures*, vol. 152, pp. 129–148, 2017.

[15] C. Yang and P. Okumus, "Ultrahigh-performance concrete for posttensioned precast bridge piers for seismic resilience,"

Journal of Structural Engineering, vol. 143, no. 12, Article ID 4017161, 2017.

[16] J. Xie, Q. Fu, and J. B. Yan, "Compressive behaviour of stub concrete column strengthened with ultra-high performance concrete jacket," *Construction and Building Materials*, vol. 204, pp. 643–658, 2019.

[17] S. Ali Dadvar, D. Mostofinejad, and H. Bahmani, "Strengthening of RC columns by ultra-high performance fiber reinforced concrete (UHPFRC) jacketing," *Construction and Building Materials*, vol. 235, Article ID 117485, 2020.

[18] Gb/T 50152-2012, *Standard for Test Method of concrete Structures*, China Architecture and Building Press, Beijing, China, 2012.

[19] S. Yuan, Z. Liu, T. Tong, and Y. Wang, "A coupled adhesive-frictional model tailored for interfacial behaviors between UHPC and NC materials," *Structures*, vol. 38, pp. 1397–1410, 2022.

[20] D. S. Simulia, *Abaqus Analysis User's Manual*, Dassault Systemes, Pawtucket, RI, USA, 2010.

[21] P. J. M. Monteiro and J. Lubliner, "A generalized continuum theory for concrete," *Cement and Concrete Research*, vol. 19, no. 6, pp. 929–938, 1989.

[22] J. Lee and G. L. Fenves, "Plastic-damage model for cyclic loading of concrete structures," *Journal of Engineering Mechanics*, vol. 124, no. 8, pp. 892–900, 1998.

[23] E. Hognestad, N. W. Hanson, and D. McHenry, "Concrete stress distribution in ultimate strength design," *Journal Proceedings*, vol. 52, no. 12, pp. 455–480, 1955.

[24] Comité Euro-International du Béton, *CEB-FIP Model Code 1990: Design Code*, Thomas Telford Publishing, London, UK, 1993.

[25] T. Tong, S. Yuan, H. Wang, Z. Liu, and J. Wang, "Numerical insights on quasi-static behaviors of UHPC-NC composite members by a phase-field approach enhanced with a cohesive-frictional interface model," *Composite Structures*, vol. 297, Article ID 115948, 2022.

[26] T. J. Hughes, G. Engel, L. Mazzei, and M. G. Larson, "The continuous Galerkin method is locally conservative," *Journal of Computational Physics*, vol. 163, no. 2, pp. 467–488, 2000.

[27] J. P. McGarry, É. Ó Máirtín, G. Parry, and G. E. Beltz, "Potential-based and non-potential-based cohesive zone formulations under mixed-mode separation and over-closure. Part I: theoretical analysis," *Journal of the Mechanics and Physics of Solids*, vol. 63, pp. 336–362, 2014.

[28] A. M. D'Altri, C. Carloni, S. de Miranda, and G. Castellazzi, "Numerical modeling of FRP strips bonded to a masonry substrate," *Composite Structures*, vol. 200, pp. 420–433, 2018.

[29] L. Snozzi and J. F. Molinari, "A cohesive element model for mixed mode loading with frictional contact capability," *International Journal for Numerical Methods in Engineering*, vol. 93, no. 5, pp. 510–526, 2013.

[30] D. W. Spring and G. H. Paulino, "Computational homogenization of the debonding of particle reinforced composites: the role of interphases in interfaces," *Computational Materials Science*, vol. 109, pp. 209–224, 2015.

[31] T. Tong, S. Yuan, J. Wang, and Z. Liu, "The role of bond strength in structural behaviors of UHPC-NC composite beams: experimental investigation and finite element modeling," *Composite Structures*, vol. 255, Article ID 112914, 2021.

[32] J. Teng, Y. L. Huang, L. Lam, and L. P. Ye, "Theoretical model for fiber-reinforced polymer-confined concrete," *Journal of Composites for Construction*, vol. 11, no. 2, pp. 201–210, 2007.

[33] J. B. Mander, M. J. Priestley, and R. Park, "Theoretical stress-strain model for confined concrete," *Journal of Structural Engineering*, vol. 114, no. 8, pp. 1804–1826, 1988.

[34] S. Popovics, "A numerical approach to the complete stress-strain curve of concrete," *Cement and Concrete Research*, vol. 3, no. 5, pp. 583–599, 1973.

[35] F. Braga, R. Gigliotti, and M. Laterza, "Analytical stress–strain relationship for concrete confined by steel stirrups and/or FRP jackets," *Journal of Structural Engineering*, vol. 132, no. 9, pp. 1402–1416, 2006.

[36] H. Kupfer, H. K. Hilsdorf, and H. Rusch, "Behavior of concrete under biaxial stresses," *Journal proceedings*, vol. 66, no. 8, pp. 656–666, 1969.